Desalination 363 (2015) 112–125

Contents lists available at ScienceDirect

Desalination

journal homepage: www.elsevier.com/locate/desal

Experimental study for hybrid humidification–dehumidification water desalination and air conditioning system

S.A. Nada [a], H.F. Elattar [a,*], A. Fouda [b]

[a] Department of Mechanical Engineering, Benha Faculty of Engineering, Benha University, Benha, 13511 Qalyubia, Egypt
[b] Department of Mechanical Power Engineering, Faculty of Engineering, Mansoura University, 35516 El-Mansoura, Egypt

HIGHLIGHTS

- A new hybrid humidification–dehumidification and air conditioning system is proposed and investigated.
- The proposed system keeps the function of the air conditioning system and uses it in water desalination.
- The effects of system operating parameters on system performance were evaluated and correlated.

ARTICLE INFO

Article history:
Received 27 September 2014
Received in revised form 19 January 2015
Accepted 22 January 2015
Available online 27 January 2015

Keywords:
Water desalination
Air conditioning
Humidification–dehumidification
Vapor compression cycle

ABSTRACT

An experimental study of the performance of a hybrid humidification–dehumidification water desalination and air conditioning system using vapor compression refrigeration cycle is presented and investigated. A test rig is designed and constructed to study the performance under different operating parameters (air flow rate, air inlet temperature, specific humidity and evaporator saturation temperature). The effects of these operating parameters on fresh (desalinated) water production rate, refrigeration capacity, compressor work per kilogram of fresh water, mass transfer coefficient and supply air conditions to conditioned space (air temperature and relative humidity) are investigated and analyzed. The results show the enhancement of the fresh water production rate, the refrigeration capacity and the compressor work per kilogram of fresh water with increasing air specific humidity and air mass flow rate. The supply air temperature and relative humidity increase remarkably with increasing fresh water rate. Experimental correlations for fresh water production rate, refrigeration capacity and compressor work per kilogram of fresh water in terms of all studied parameters are deduced and presented within accepted error.

1. Introduction

There is a lack of drinkable water in most of hot and humid environment regions around the world. At the same time, these regions need air conditioning systems for thermal comfort. Nowadays, many of the countries depend on water desalination systems to supply their water demands. Atmospheric water vapor processing (AWVP) is a recent technology of fresh water production, especially for hot and humid climates. Nevertheless, produced fresh water is slightly compared to the present methods; it is a choice to be studied for low water demand regions [1]. Aly et al. [2] studied theoretically and experimentally the performance of the mechanical vapor compression (MVC) desalination system. Siqueiros and Holland [3] proposed desalination systems operated by heat pumps (mechanical vapor compression and/or absorption machines) as a compact and less cost structure that has first been used for the dry areas in north of Mexico. Additionally, the reasonable economic potential is given as compared to reverse osmosis technology. Hawlader [4] studied and described a novel solar-assisted heat pump desalination system and a good water production was obtained. Slesarenko [5] suggested incorporating heat pumps as a source of heat energy for seawater desalination plants. Two plants were proposed: desalination plant with compression heat pump operated with R12 and a steam and water cycle plant. Al-Juwayhel et al. [6] used a combined vapor compression heat pump with a single effect evaporator desalination system for atmospheric water vapor condensation on the evaporator surface. The performance of a new type of a humidification–dehumidification desalination unit driven by mechanical vapor compression pump was mathematically analyzed by Gao et al. [7]. Yuan et al. [8] presented an integrative unit for air-conditioning and desalination driven by vapor compression heat pump on basis of direct humidification–dehumidification process. Performance study of a combined heat pump (HP) with a dehumidification process to produce fresh water from the atmospheric air was analyzed by Habeebullah [9]. A

* Corresponding author.
E-mail address: hassanelattar@yahoo.com (H.F. Elattar).

http://dx.doi.org/10.1016/j.desal.2015.01.032
0011-9164/

Nomenclature

A	Total surface area, m^2
A_{min}	Minimum air flow area, m^2
A_o	Total coil surface area, m^2
D_h	Coil hydraulic diameter ($D_h = 4L_d\ A_{min}/A_o$), m
h_m	Mass transfer coefficient, m/s
$h_{fg,0\ °C}$	Latent heat of evaporation of water at 0 °C, kJ/kg
i	Specific enthalpy, kJ/kg
L_d	Coil depth, m
$\dot{m}$	Mass flow rate, kg/s
$\dot{m}_{steam}$	Steam mass flow rate, kg/s
$\dot{Q}_{ref}$	Refrigeration capacity, kW
$\dot{Q}_{ref,\,l}$	Refrigeration capacity–latent part, kW
P	Gauge pressure, Pa
RH	Air relative humidity, dimensionless
Re_{Dh}	Reynolds number based on hydraulic diameter
t	Temperature, °C
t_{amb}	Equivalent dry bulb temperature of inlet state, °C
u_a	Air velocity, m/s
w	Air specific humidity, $g_{water}/kg_{dry\ air}$
$\dot{W}_c$	Actual compressor work, kW

Greek symbols

η_{ic}	Overall compressor efficiency
μ	Dynamic viscosity, N s/m^2
$\rho_{v,a}$	Moist air water vapor density, kg/m^3
$\rho_{v,su}$	Water vapor density at evaporator surface, kg/m^3

Subscript

a	Air
c	Compressor
ev	Evaporator
i	Inlet
o	Outlet
r	Refrigerant
s	Evaporator saturation temperature
w	Fresh water

patented layer freezing based technology which is scalable and coupled with a heat pump to switch freezes water from seawater in the evaporator and melts the ice in the subsequent phase when it serves as a condenser that was discussed by Rane and Padiya [10]. Heat pumps using agent R12 or water and vapor to be used as a source of heat energy for seawater desalination were introduced by Jinzeng and Huang [11]. An experimental evaluation of a two-stage technique to improve the humidification–dehumidification process in fresh water production from brackish water was presented by Zamen et al. [12]. The investigation of the potential for heat recovery from Multi Stage Flash (MSF) desalination plant hot distillate water to power an Organic Rankine Cycle (ORC), comparing R134a and R245fa refrigerants as the working fluid addressed by Al-Weshahi et al. [13]. Theoretical study of a simple solar still coupled to a compression heat pump was presented by Halima et al. [14]. The mathematical model has been developed using mass and heat balance. A new concept of produced water purification by humidification–dehumidification (HD) process in which low-temperature energy sources, such as co-produced geothermal energy or solar energy that could be used to drive the water desalination process was developed by Xinhua Li [15]. An open air–vapor compression refrigeration system for both air-conditioning and desalination on ship cooled by seawater was presented by Houa et al. [16]. An experimental investigation for dehumidification process of a wavy-finned-tube direct expansion cooling coil under humid condition was carried out by Huzayyin et al. [17]. Shen et al. [18] presented a comprehensive analysis of a single-effect mechanical vapor compression (MVC) desalination system using water injected twin screw compressors. The operational characteristics of the twin screw compressor including inlet volume flow rate, compressor pressure ratio and mass fraction of the injected water were investigated. Ghazal et al. [19] presented an experimental investigation for the performance of a solar humidification prototype that is suitable for using in humidification–dehumidification desalination (HDD) systems. Attia [20] introduced a new proposed system that depends on the optimization of utilizing the heat flow of the heat pump system to increase the whole system efficiency. Al-Ansari et al. [21] modeled and analyzed a single effect evaporation desalination process combined with adsorption heat pump (ADVC) in terms of designed and operational system parameters. Nafey et al. [22] presented a numerical investigation of a humidification–dehumidification desalination (HDD) process using solar energy. Nafey et al. [23] presented an experimental investigation for desalination system based on humidification–dehumidification desalination (HDD) technique using solar energy at the weather conditions of Suez City, Egypt.

According to authors' review, there is a shortage in the utilization of air conditioning systems in fresh water production by incorporating humidification–dehumidification desalination to the system with keeping the function of air conditioning systems (maintain human thermal comfort). Therefore, the present study introduces hybrid air conditioning and humidification–dehumidification desalination system to produce fresh water and satisfy the required thermal comfort conditions inside the conditioned space. In the study, the effects of the different system operating conditions (air mass flow rate, evaporator air inlet temperature, evaporator air inlet specific humidity and the evaporator saturation temperature) on the supply air conditions to conditioned space, desalinated water production rate, mass transfer coefficient, evaporator refrigeration capacity and compressor work per kilogram of fresh water are experimentally investigated to evaluate the feasibility of the system at the different operating conditions.

2. Experimental setup description and instrumentation

The experimental setup was designed to be consists of four independent main loops (refrigerant, humid air, fresh water and sea water loops) to enable the investigation of the effects of the operating conditions on the conditioned space-supplied air conditions, fresh water production rate, refrigeration capacity, compressor work per kilogram of fresh water and mass transfer coefficient.

2.1. Experimental setup description

Fig. 1 illustrates a schematic diagram of the experimental setup. The main system components are air blower (1), air heaters (2), steam boiler (10), humidifier (steam distributer) (3), evaporator (cooler and dehumidifier) (7). The setup includes the measuring and instrumentation devices to measure the different parameters needed for the study (temperatures, relative humidities, and air flow rates). The system consists of four loops, one closed loop for refrigerant, and the others are open loops for air, fresh water and sea water. In the refrigerant loop, refrigerant R134a is used. As shown in Fig. 1, the loop consists of compressor, oil separator condenser, liquid receiver, expansion device (automatic expansion valve, AEV), filter drier, heat exchanger, evaporator and suction line accumulator. The evaporator is a wavy-finned tube coil and it consists of three tube rows in staggered arrangement with 304.8 mm × 228.6 mm face area as shown in Fig. 2. The evaporator dimensions and specifications are given in Table 1. Air is flowing over evaporator surface passing through its fins where the cooling and dehumidification process is conducted. The evaporator pressure and corresponding saturation temperature varies with changing inlet air conditions and mass flow rate to verify system balance [24,25].

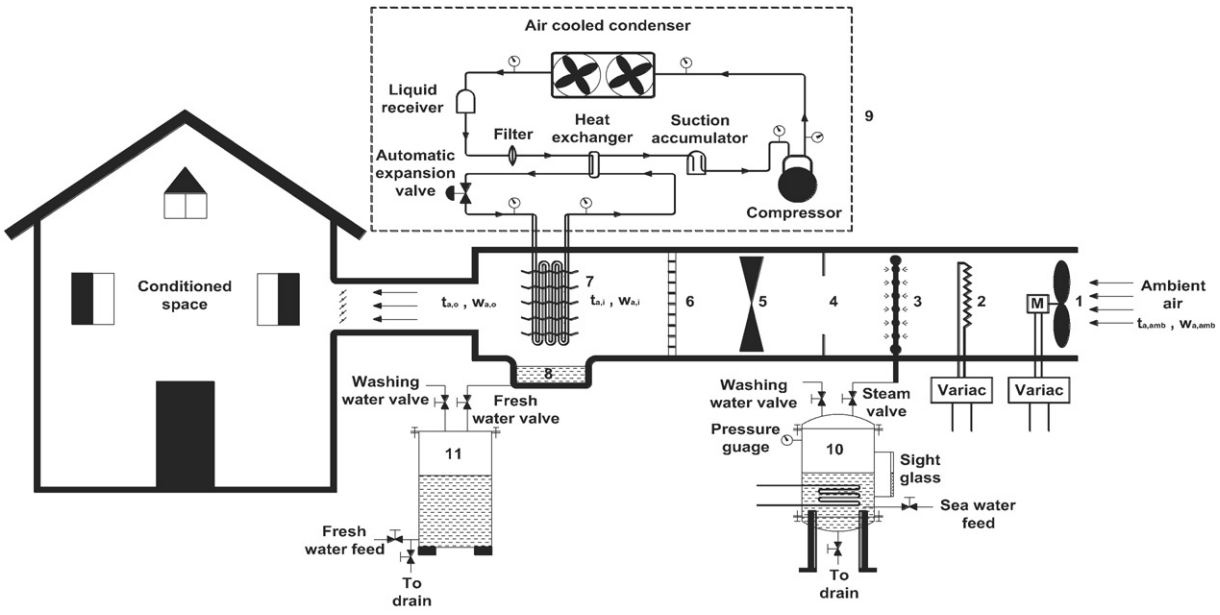

Fig. 1. Schematic diagram of experimental setup. 1. Air blower; 2. Air heaters; 3. Humidifier; 4. Orifice meter; 5. Air mixer; 6. Straightener; 7. Evaporator; 8. Fresh water basin; 9. Refrigeration unit; 10. Steam boiler; and 11. Fresh water storage tank.

Therefore, automatic expansion valve (AEV) type is used in the present study for easy adjustment of evaporator pressures in case of its changing with the changes of air inlet conditions. Consequently, the evaporator saturation temperature is maintained constant according to the adjusted pressure. The amount of refrigerant superheat inside the evaporator changes with inlet air conditions to retain the evaporator pressure and corresponding saturation temperature.

In addition to that, the refrigerant pressure drop inside the evaporator was measured at all the studied variable ranges. It was in around 7 kPa (corresponding to $\Delta T_s \cong 0.5$ °C). Therefore, the evaporator pressure and corresponding saturation temperature was assumed to be constant at the evaporator inlet during all the experiments.

In the air loop, air is withdrawn from the ambient by air blower (1) connected by variable transformer (Variac) to control air mass flow rate. Subsequently, the air flows over three air heaters (3 kW each) distributed in staggered shape for covering the entire flow cross section area. The heaters are connected to a variac (variable transformer) to vary input power and consequently control air temperature. The air is then passed through a humidifier (steam distributor) (3) to humidify the air and control its humidity. The geometry of the humidifier was designed to cover the entire flow cross section area to obtain uniform humidity distribution at the entrance of the evaporator. After that the air flows through an orifice meter (4) to measure the air velocity by using a differential pressure manometer. The air is then passed

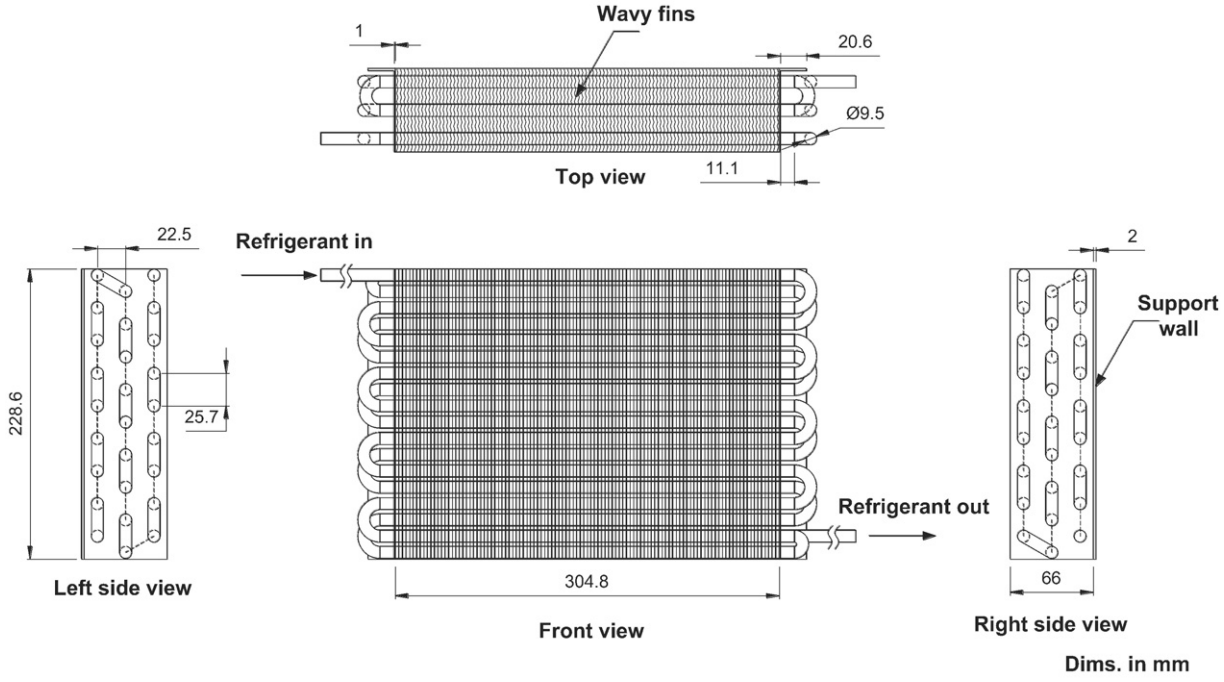

Fig. 2. Evaporator (cooler and dehumidifier).

Table 1
Evaporator dimensions and specifications.

Parameters	Values
Evaporator dimensions	
Width	304.8 mm
Height	228.6 mm
Depth	65.989 mm
Face area	0.06968 m^2
Actual flow area	0.041395 m^2
Total external surface area	3.2621 m^2
Tubes specifications	
Number of tube rows	3
Number of tubes in each row	9
Tube material	Copper
Tube arrangement	Staggered
Length of straight tube	304.8 mm
Transverse tube spacing	22.475 mm
Longitudinal tube spacing	25.715 mm
Outside tube diameter	9.525 mm
Inside tube diameter	8.712 mm
Fins specifications	
Type	Wavy
Material	Aluminum
Thickness	0.1397 mm
Collar diameter	9.8044 mm
Number	108
Pitch	9 fins/in.
Wavelength	6.5 mm
Wave height	1 mm
Corrugation angle	17°

through air mixer (5) followed by flow straighteners (6) to maintain uniform air velocity, air temperature, and air humidity at the entrance of the evaporator (7). The air is then cooled and dehumidified in the evaporator section before supplying it to the conditioned space.

In the fresh water loop, water vapor is condensed over the evaporator (7) surface, then collected and measured in fresh water basin (8) then it stored in a fresh water storage tank (11). In the sea water loop, sea water enters the steam boiler (10) with a steady rate, where it is heated and evaporated. The generated steam is then passed through the humidifier (steam distributer) (3) to humidify the air. In order to adjust the air humidity to the tested values, the boiler capacity was controlled by controlling the input electric power. Boiler washing process is necessary regularly to reduce the salt concentration inside the boiler.

2.2. Instrumentations

The operational parameters which are necessary to investigate the system performance are measured by measuring instruments including thermocouples connected with data acquisition system and a PC, orifice meter with digital differential pressure manometer, digital thermohygrometers and pressure gauges. The thermocouples which used are K-type (Chromele Alumel) having 0.5 mm diameter and calibrated using standard thermometer with ±0.2 °C accuracy. Two groups (9 thermocouples each) of thermocouples and two other wetted cotton bulb thermocouples are arranged upstream and downstream of the evaporator to measure the air dry and wet-bulb temperatures, respectively. Another five thermocouples are used to measure the temperatures at various locations: the refrigerant inlet and exit of the evaporator tubes, the refrigerant tube surface at the entrance of the expansion device and the other two thermocouples were used to measure the ambient dry and wet-bulb temperatures. For logging the thermocouple reading, all thermocouples are connected to a data acquisition system and a PC through extension wires. An orifice meter with a digital differential pressure manometer is used to measure the air velocity using the equal area traverse method to calculate the average air velocity and consequently the air mass flow rate. A hotwire anemometer was used to calibrate the orifice meter by measuring the air velocity distribution through the flow cross section and recording the pressure drop across the orifice at the same time. Two digital thermohygrometers are used to measure evaporator upstream and downstream air relative humidity. Six pressure gauges with different ranges are used to show the refrigerant pressures at inlet and outlet of the compressor, the condenser, and the evaporator. Another pressure gauge is used to indicate the boiler pressure. The detailed technical specifications of instruments which are used in experimental setup are presented in Table 2.

3. Experimental procedure and data processing

3.1. Experimental procedure and conditions

The procedure and experimental program are as follows:

- Adjusting the evaporator pressure to the required value.
- Adjusting the air frontal velocity to achieve the required mass flow rate.
- Adjusting the air inlet temperature to the required value.
- Adjusting the air inlet relative humidity to the required value.
- Waiting until steady state was achieved. It was found that this take about 15 to 30 min depending on the air velocity.
- Recording the readings of all thermocouples, pressure drop across the orifice flow meter, relative humidity upstream and downstream of the evaporator and frontal air velocity. The readings have been recorded after steady state condition was maintained (i.e. at constant values).
- Repeating the above steps with different operating conditions according to the following ranges:

Air inlet temperature 20–30 °C
Air inlet relative humidity 40–95%
Frontal air velocity 0.5–1.5 m/s (within the range recommended by ASHRAE) [26]
Evaporator gauge pressure 308–377 kPa (t_s = 1.388–7.167 °C).

3.2. Data processing

The fresh water production rate, refrigeration capacities (total and latent) and the injected steam mass flow rate are calculated from the measurements of air properties just upstream and downstream of the evaporator and the refrigerant properties at evaporator inlet and outlet as follows:

$$\dot{m}_w = \dot{m}_a\left(w_{a,i} - w_{a,o}\right) \tag{1}$$

$$\dot{Q}_{ref} = \dot{m}_a\left(i_{a,i} - i_{a,o}\right) = \dot{m}_r\left(i_{r,ev,o} - i_{r,ev,i}\right) \tag{2}$$

$$\dot{Q}_{ref,l} = \dot{m}_w \; h_{fg,0^oC} \tag{3}$$

$$\dot{m}_{steam} = \dot{m}_a\left(w_{a,i} - w_{a,amb}\right). \tag{4}$$

The air specific humidities and enthalpies and refrigerant enthalpies that illustrated in Eqs. (1)–(4) are calculated from air and refrigerant

Table 2
Instrumentations technical specifications.

Instrumentation	Range	Accuracy
K-type thermocouple	−200 to 1250 °C	±0.2 °C
Digital differential pressure manometer	±2 bar	±2%
Digital thermohygrometer	5% to 98% RH	±0.1% RH
	−10 °C to 70 °C	±0.1 °C
Pressure gauges (refrigeration unit)	−100 to 2400 kPa	±1%
Pressure gauge (steam boiler)	0 to 16 bar	±1%

property measurements. Compressor work, refrigeration unit coefficient of performance, mass transfer coefficient and Reynolds number over the evaporator surface are calculated from the following equations:

$$\dot{W}_c = \dot{m}_r\left(i_{r,c,o} - i_{r,c,i}\right) \tag{5}$$

$$COP = \frac{\dot{Q}_{ref}}{\dot{W}_c} \tag{6}$$

$$h_m = \frac{\dot{m}_w}{A_{ev}\left(\rho_{v,a} - \rho_{v,su}\right)} \tag{7}$$

$$\mathrm{Re}_{D_h} = \frac{\rho_a u_a D_h}{\mu_a}. \tag{8}$$

The performance of the system is studied by solving the previous system of equations (Eq. (1) to Eq. (8)) using EES (Engineering Equation Solver, commercial version 6.883-3D) software and all air and refrigerant properties are determined from EES by using the measured parameters.

Eqs. (1)–(7) can be put on the form $R = f(x_1, x_2, x_3,\ldots, x_n)$ where R is the calculated variable and $(x_1, x_2, x_3,\ldots,x_n)$ are the measured parameters. The errors in the measurements of these parameters are depicted in Table 2. The uncertainty in R due to the uncertainties of these parameters can be calculated from Eq. (9) that was given by Holman and Gajda [27].

$$\frac{\Delta R}{R} = \left[\left(\frac{\partial R}{\partial X_1}\frac{\Delta X_1}{R}\right)^2 + \left(\frac{\partial R}{\partial X_2}\frac{\Delta X_2}{R}\right)^2 + \ldots + \left(\frac{\partial R}{\partial X_N}\frac{\Delta X_N}{R}\right)^2\right]^{\frac{1}{2}} \tag{9}$$

where $\partial R/\partial x_i$ is calculated by numerical differentiation using the developed computer program. The minimum and maximum uncertainty in $\dot{m}_w$, h_m, $\dot{Q}_{ref}$, $\dot{W}_c$, and COP for all the data are found to be (2.7 and 11.4%), (0.6 and 11.3%), (2.5 and 11.2%), (2.9 and 13.8%), and (0.4 and 0.7%), respectively.

4. Results and discussion

The results of the present work are analyzed and discussed to investigate the effects of the operating conditions on the fresh water production rate, refrigeration capacity, compressor work per kilogram of fresh water, mass transfer coefficient and conditioned space-supplied air conditions (air temperature and relative humidity).

4.1. Fresh water rate and mass transfer coefficient

4.1.1. Fresh (desalinated) water production rate

Fig. 3a–c shows the variation of the fresh water production rate ($\dot{m}_w$) against air specific humidity ($w_{a,i}$) with air mass flow rate ($\dot{m}_a$) as a parameter for evaporator saturation temperature t_s = 1.388 °C (P_{ev} = 308 kPa) and at different evaporator air inlet temperatures $t_{a,i}$ = 20, 25 and 30 °C, respectively. As shown in the figure for any air mass flow rate and air inlet temperature, the fresh water production rate increases with increasing air specific humidity. This can be attributed to the increase of air relative humidity with increasing air specific humidity at constant $t_{a,i}$. Accordingly, the mass transfer to the evaporator surface increases and this increases the condensation rate and the fresh water production rate. Additionally, an increase in $\dot{m}_w$ with increasing in $\dot{m}_a$ can be obtained at any $t_{a,i}$ and a significant increasing can be seen at $t_{a,i}$ = 25 °C and 30 °C as illustrated in Fig. 3-b and c. This is due to the increase of the mass transfer between the air and the evaporator surface in addition to the increase of renewing contact air on the evaporator surface and both cause an increase in fresh water production rate.

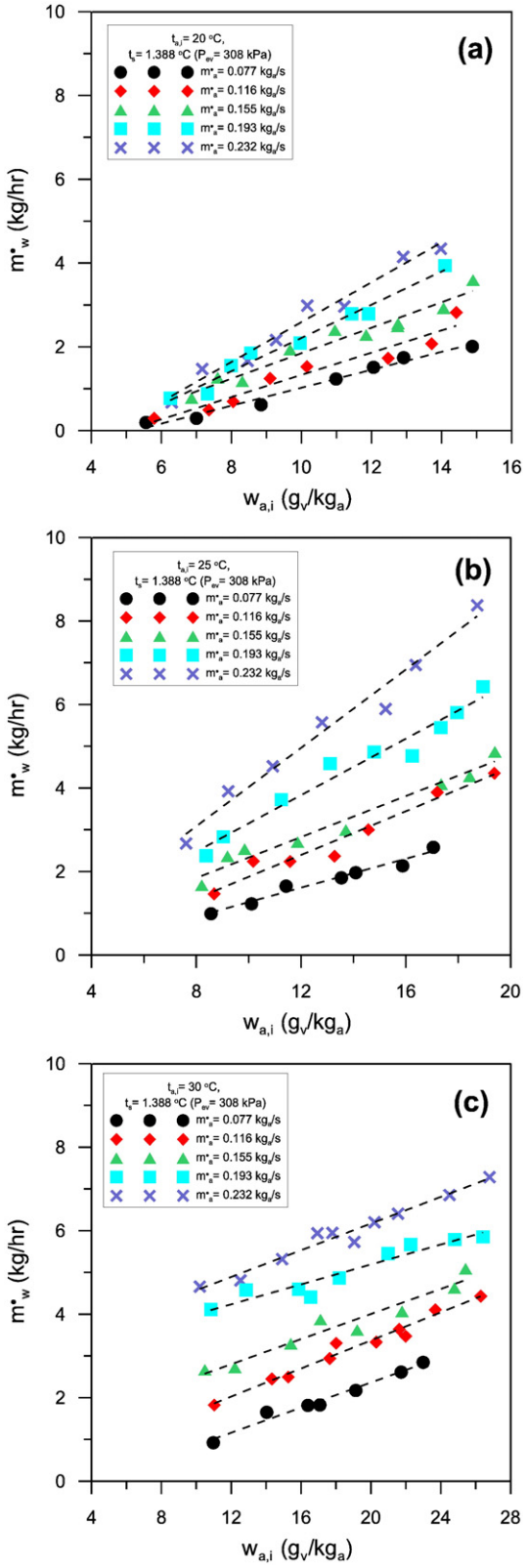

Fig. 3. Effect of air inlet specific humidity and air mass flow rate on the fresh water rate at: (a) $t_{a,i}$ = 20 °C, (b) $t_{a,i}$ = 25 °C, (c) $t_{a,i}$ = 30 °C.

The effects of the evaporator air inlet temperature and evaporator saturation temperature on the fresh water production rate are shown in Fig. 4a and b, respectively. As shown in Fig. 4a, the fresh water production rate increases as the air inlet temperature increases in the range of 20 °C ≤ $t_{a,i}$ ≤ 25 °C then it decreases at $t_{a,i}$ > 25 °C. The increase

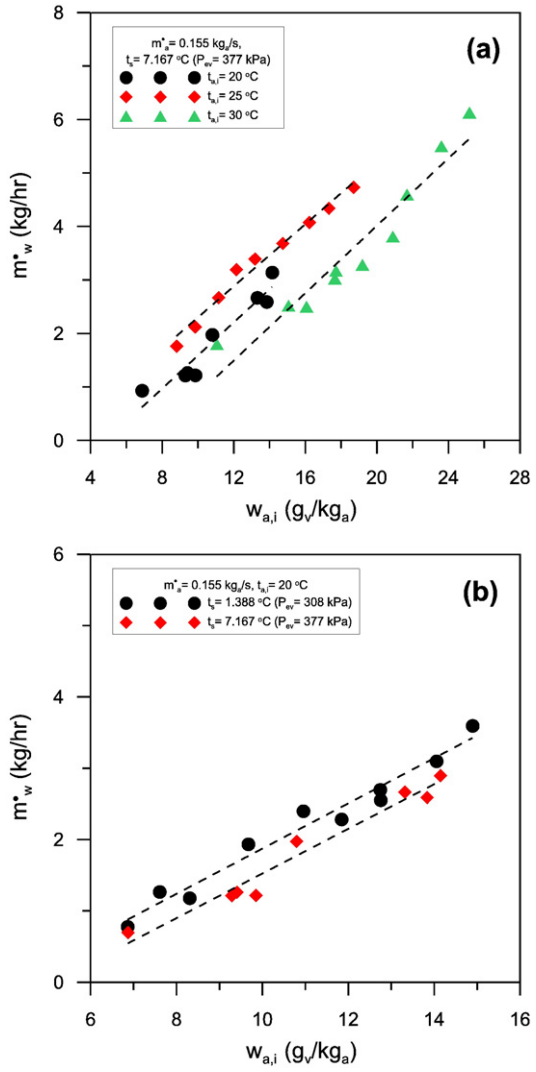

Fig. 4. Variation of fresh water rate against air inlet specific humidity: (a) Effect of evaporator air inlet temperature, (b) Effect of evaporator saturation temperature.

of $m^{\bullet}_{w}$ with increasing $t_{a,i}$ within the range of 20–25 °C can be attributed to the increase of the temperature difference between $t_{a,i}$ and t_s which improves the vapor mass transfer between air and evaporator surface. The decrease of the fresh water production rate with the increase of $t_{a,i}$ within the range of 25 °C < $t_{a,i}$ ≤ 30 °C can be attributed to (i) the reduction in the water vapor pressure difference between the air and evaporator surface as a result of the increase of the evaporator surface temperature, and (ii) the re-evaporation of part of water vapor condensate on the evaporator surface with the increase of $t_{a,i}$. Fig. 4b also shows the decrease of the fresh water production rate with increase of the evaporator saturation temperature. This can be attributed to the increase of the apparatus dew point (t_s) that causes a decrease in the specific humidity difference across the evaporator.

4.1.2. Mass transfer coefficient

Fig. 5a–c shows the variation of the mass transfer coefficient (h_m) against air specific humidity ($w_{a,i}$) with air mass flow rate ($m^{\bullet}_{a}$) as a parameter at evaporator saturation temperature t_s = 1.388 °C (P_{ev} = 308 kPa) for different evaporator air inlet temperatures, $t_{a,i}$ = 20, 25 and 30 °C, respectively. As shown in the figures the mass transfer coefficient decreases with increasing air specific humidity for any air mass flow rate and evaporator air inlet temperature. This can be attributed to the increase of air water vapor pressure overcoming the increase in the rate of condensate. Moreover, h_m decreases significantly versus $w_{a,i}$ with increasing $t_{a,i}$ and $m^{\bullet}_{a}$ as illustrated in Fig. 5b and c. This can be attributed to that at higher $t_{a,i}$ and $m^{\bullet}_{a}$, part of water condensate re-evaporates and at the same time the evaporator surface temperature increases and both reduce water condensate and potential of mass transfer to the evaporator surface.

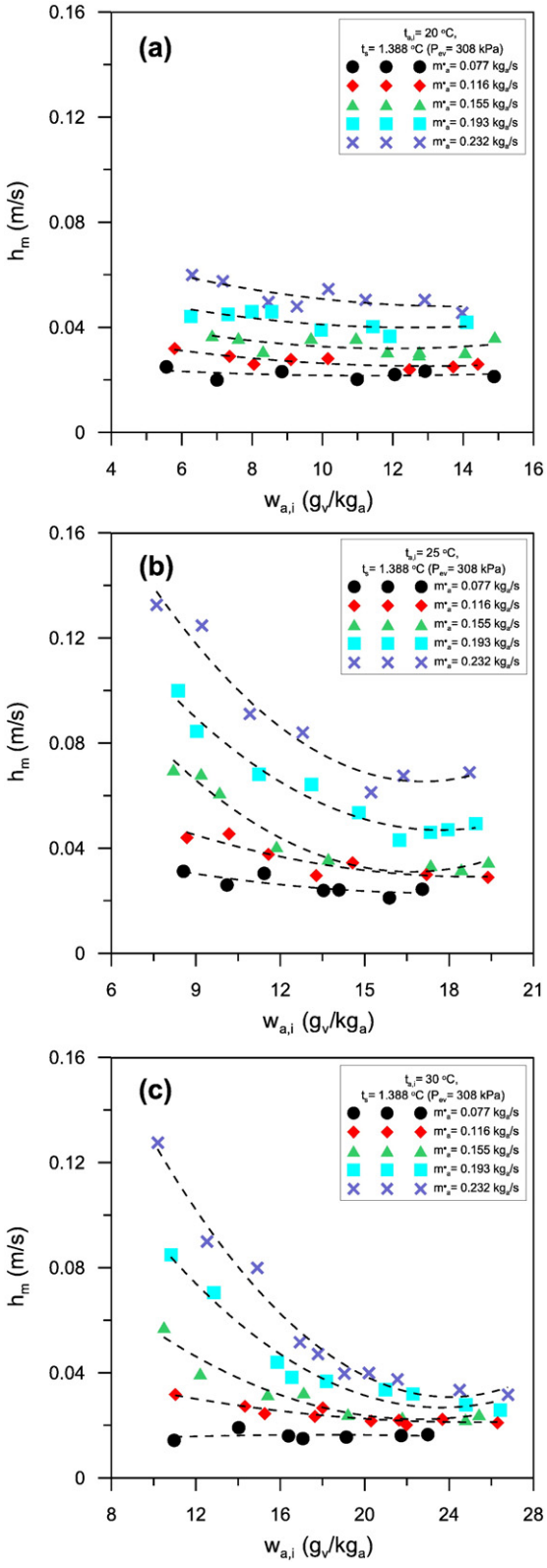

Fig. 5. Effect of air inlet specific humidity and air mass flow rate on the mass transfer coefficient at: (a) $t_{a,i}$ = 20 °C, (b) $t_{a,i}$ = 25 °C, (c) $t_{a,i}$ = 30 °C.

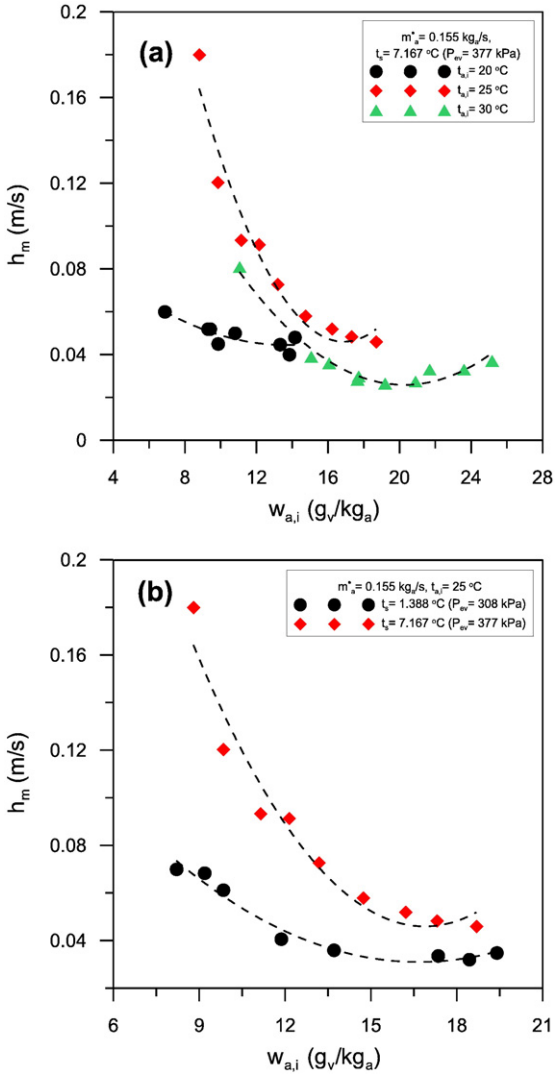

Fig. 6. Variation of mass transfer coefficient against air inlet specific humidity: (a) Effect of evaporator air inlet temperature, and (b) Effect of evaporator saturation temperature.

The effects of $t_{a,i}$ and t_s on the mass transfer coefficient are shown in Fig. 6a and b, respectively. As shown in Fig. 6a, h_m enhances as the air inlet temperature increases in the range of 20 °C ≤ $t_{a,i}$ ≤ 25 °C then h_m decreases for $t_{a,i}$ > 25 °C. This can be attributed to the same declaration as it was explained in Fig. 4a. Furthermore, h_m decreases with the decrease of t_s as can be seen in Fig. 6b and this can be attributed to the decrease of the condensate rate as t_s rises.

4.2. Evaporator refrigeration capacity

4.2.1. Evaporator total refrigeration capacity

Fig. 7a–c shows the variation of the total evaporator refrigeration capacity ($\dot{Q}_{ref}$) versus air specific humidity ($w_{a,i}$) with air mass flow rate ($\dot{m}_a$) as a parameter at t_s = 1.388 °C (P_{ev} = 308 kPa) and for different evaporator air inlet temperatures, $t_{a,i}$ = 20, 25 and 30 °C, respectively. As shown in Fig. 7, $\dot{Q}_{ref}$ augments with rising air specific humidity and the trend is the same for any $\dot{m}_a$ and $t_{a,i}$. The possible explanation is that an increase of air specific humidity at constant $t_{a,i}$ increases the latent heat part leading to the increase of the total evaporator refrigeration capacity. Also Fig. 7 shows an increase in $\dot{Q}_{ref}$ with increasing $\dot{m}_a$ at any $t_{a,i}$. The increase is significant at $t_{a,i}$ = 25 °C and 30 °C (Fig. 7-b and c). This can be attributed to the increase of heat and mass transfer coefficients as air Reynolds number increases with increasing air mass flow rate.

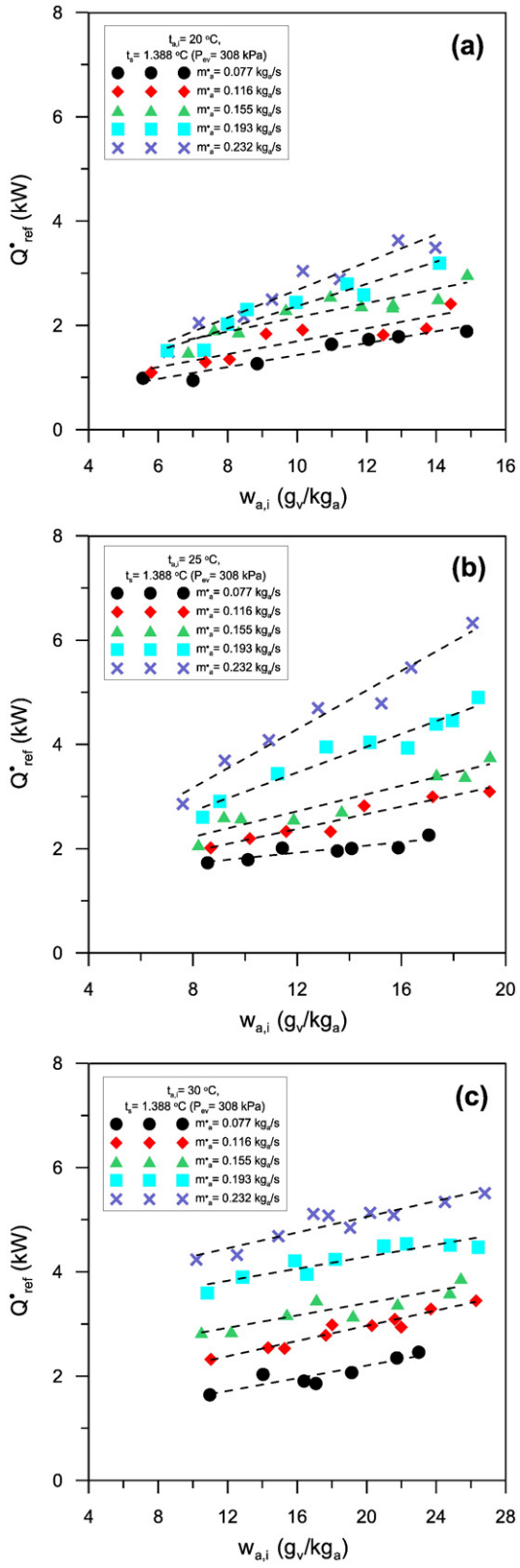

Fig. 7. Effect of air inlet specific humidity and air mass flow rate on the evaporator refrigeration capacity at: (a) $t_{a,i}$ = 20 °C, (b) $t_{a,i}$ = 25 °C and (c) $t_{a,i}$ = 30 °C.

The effects of the evaporator air inlet and saturation temperatures on $\dot{Q}_{ref}$ are presented in Fig. 8a and b, respectively. As shown in Fig. 8a, $\dot{Q}_{ref}$ increases as air inlet temperature increases within the range of 20 °C ≤ $t_{a,i}$ ≤ 25 °C then $\dot{Q}_{ref}$ decreases at $t_{a,i}$ > 25 °C. The

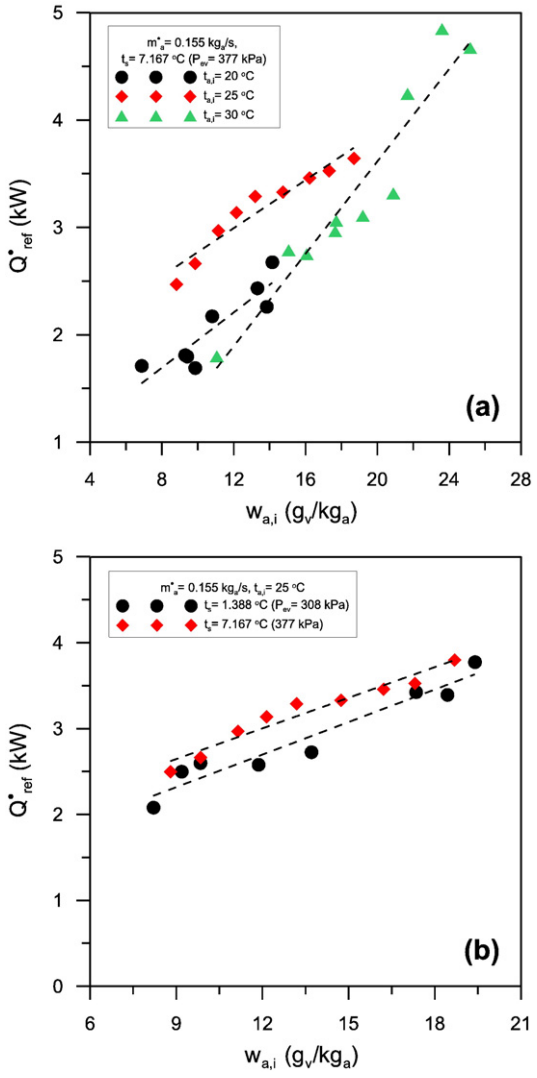

Fig. 8. Variation of evaporator refrigeration capacity against air inlet specific humidity: (a) Effect of evaporator air inlet temperature, (b) Effect of evaporator saturation temperature.

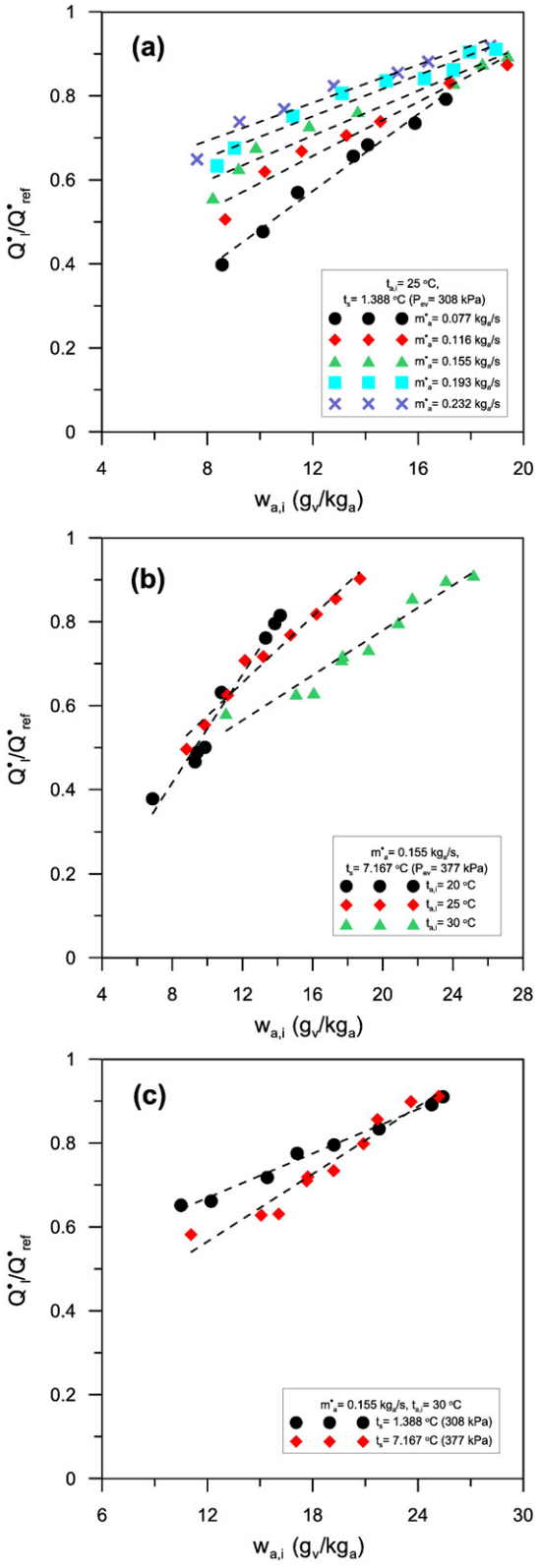

Fig. 9. Variation of latent to total refrigeration capacity ratio against air inlet specific humidity: (a) Effect of air mass flow rate, (b) Effect of evaporator air inlet temperature, and (c) Effect of evaporator saturation temperature.

increase of $Q^{\bullet}_{ref}$ with increasing $t_{a,i}$ in the range of $t_{a,i} = 20$–25 °C can be attributed to the increase of the enthalpy difference across the evaporator as a result of increasing in $t_{a,i}$ which improves the heat transfer rate between air and evaporator surface. Conversely, $Q^{\bullet}_{ref}$ decreases with increasing $t_{a,i}$ within the range of 25 °C < $t_{a,i} \leq 30$ °C, can be attributed to the reduction of enthalpy difference across the evaporator with increasing evaporator surface temperature (i.e. sensible heat part reduces). Furthermore, latent heat part decreases due to the increase of water condensate re-evaporation with increasing $t_{a,i}$ and both cause a drop off in evaporator refrigeration capacity as a result of increasing evaporator air outlet enthalpy. As shown in Fig. 8b, the evaporator refrigeration capacity increases with the evaporator saturation temperature. This owing to the increase in the apparatus dew point (t_s) that causes a raise in the air enthalpy difference across the evaporator (i.e. small superheated region occurred in the evaporator).

4.2.2. Evaporator latent refrigeration capacity

Fig. 9a–c shows the variation of latent to total refrigeration capacity ratio ($Q^{\bullet}_l/Q^{\bullet}_{ref}$) against the evaporator air inlet specific humidity with the air mass flow rate, evaporator air inlet temperature and evaporator saturation temperature as parameters, respectively. As shown in Fig. 9a, $Q^{\bullet}_l/Q^{\bullet}_{ref}$ increases with increasing air specific humidity for any $m^{\bullet}_a$. This is due to the same declaration that was explained in discussion of Fig. 7. Fig. 9b shows the increase of $Q^{\bullet}_l/Q^{\bullet}_{ref}$ with increasing $t_{a,i}$ and this is

because of rising in sensible heat part due to raising of $t_{a,i}$ and consequently a decay in latent heat part for the same evaporator refrigeration capacity. Fig. 9c shows the decrease of $\dot{Q}_l/\dot{Q}_{ref}$ with the increase of the evaporator saturation temperature. This can be attributed to the increase of apparatus dew point (t_s) that reduces the difference of air specific humidity across the evaporator.

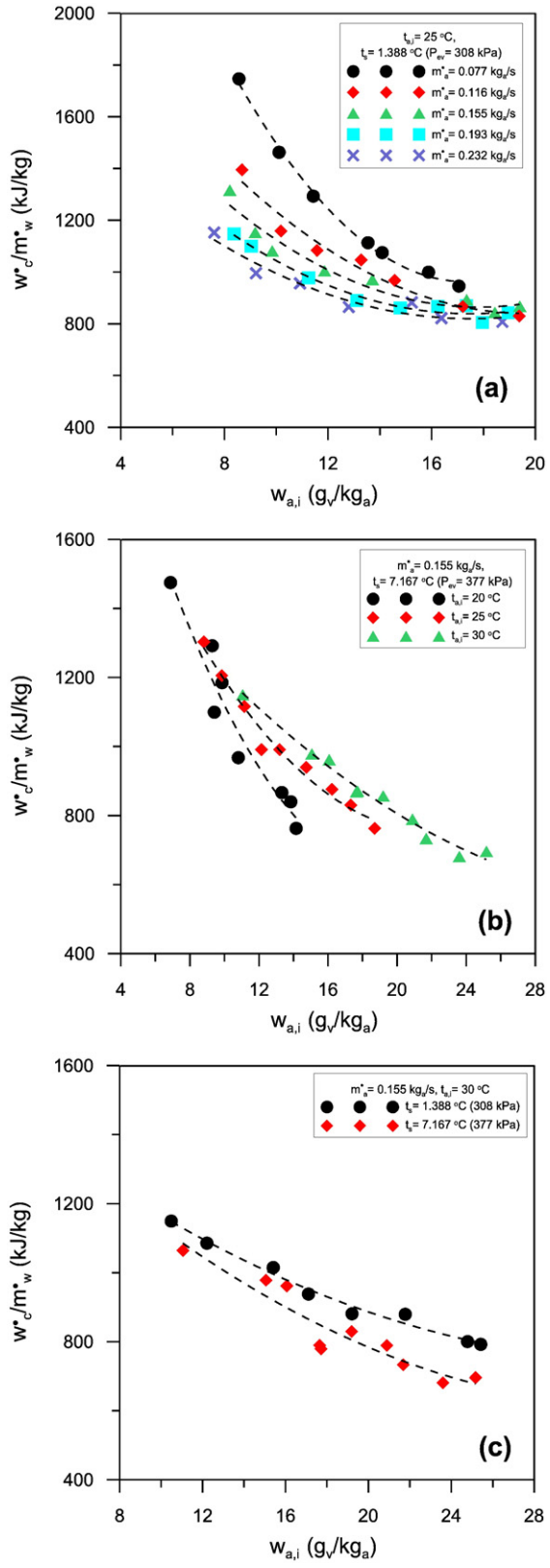

Fig. 10. Variation of compressor work per kilogram of fresh water against air inlet specific humidity: (a) Effect of air mass flow rate, (b) Effect of evaporator air inlet temperature, and (c) Effect of evaporator saturation temperature.

4.3. Compressor power analysis and COP

4.3.1. Refrigeration unit compressor work

Fig. 10a–c shows the variation of the compressor work per kilogram of fresh water (W^*_c/m^*_w) versus air inlet specific humidity with air mass flow rate, evaporator air inlet temperature and evaporator saturation temperature as parameters, respectively. As shown in Fig. 10a, W^*_c/m^*_w decreases with increasing air specific humidity and m^*_a. This is due to the increase of the fresh water production rate with the increase of the air specific humidity and consequently the increase of the latent heat which leads to the increase of the compressor power but the increase in the fresh water production rate overcomes on the increase in compressor power and this leads to dropping in W^*_c/m^*_w with increasing $w_{a,i}$ and m^*_a.

Fig. 10b shows that W^*_c/m^*_w increases with increasing $t_{a,i}$ for any air specific humidity. This is owing to the increasing in sensible heat part for higher $t_{a,i}$, hence the compressor power rises without changing in the fresh water production rate. Furthermore, W^*_c/m^*_w decreases as the evaporator saturation temperature increases as shown in Fig. 10c. The possible explanation is that the reduction in m^*_w and W^*_c is due to the increase in the evaporator saturation temperature but the reduction in W^*_c overcomes the reduction in m^*_w and this leads to a drop in W^*_c/m^*_w with increasing t_s.

4.3.2. Refrigeration unit COP

The variation of the coefficient of performance (COP) against air inlet specific humidity with m^*_a, $t_{a,i}$ and t_s as parameters is presented in Fig. 11a–c, respectively. It is observed that, $w_{a,i}$, m^*_a and $t_{a,i}$ have approximately negligible effects on COP at constant t_s (see Fig. 11a and b). This is due to that the variations in $w_{a,i}$, m^*_a and $t_{a,i}$ cause a reasonable change on $\dot{Q}_{ref}$ and this leads to a change in the condenser pressure and consequently W^*_c. The change in $\dot{Q}_{ref}$ has approximately equals to the change in W^*_c, and this maintains COP constant. On the other hand, Fig. 11c shows that the evaporator saturation temperature has a significant influence on COP, where the COP decreases with the dropping of t_s. This can be attributed to the increase of W^*_c with the dropping in t_s and this leads to a reduction in COP.

4.4. Conditions of the supply air to the conditioned space

In order to see the conditions of supply air to the conditioned space ($t_{a,o}$ and $RH_{a,o}$) at any fresh water rate m^*_w (both of them are system results and depend on the operating system parameters) the variations of $t_{a,o}$ and $RH_{a,o}$ versus m^*_w with m^*_a, $t_{a,i}$ and t_s as parameters are presented in Fig. 12a–f, respectively. As shown in the figure $t_{a,o}$ and $RH_{a,o}$ increase remarkably with increasing m^*_w and the trends are the same for any m^*_a, $t_{a,i}$ and t_s. The possible explanation is the decrease of the grand sensible heat factor with the increase of the condensate rate and this leads to the increase of $t_{a,o}$ and $RH_{a,o}$. At the same time, the thermal resistance of condensate layer on the evaporator surface increases with increasing the rate of condensate and this reduces heat transfer rate which leads to higher $t_{a,o}$. The effect of m^*_a is considerable on $t_{a,o}$ and $RH_{a,o}$, where $t_{a,o}$ rises and $RH_{a,o}$ drops as m^*_a increases. This can be attributed to the reduction of the sensible heat part with increasing m^*_a as can be seen in Fig. 12a and b. Furthermore, $t_{a,i}$ has a reasonable influence on $t_{a,o}$ and $RH_{a,o}$, where $t_{a,o}$ increases and $RH_{a,o}$ decreases with increasing $t_{a,i}$ in the range of $t_{a,i}$ = 20–25 °C and then increases in the range of $t_{a,i}$ = 25–30 °C. The trend is the same for any m^*_w as shown in Fig. 12c and d. This can be attributed to the unchanging in the evaporator sensible heat part with increasing of $t_{a,i}$ and this results in an increase in $t_{a,o}$. On the other hand, in the range of $t_{a,i}$ = 20–25 °C, $RH_{a,o}$ decreases due to increasing of $t_{a,o}$ but in the range of $t_{a,i}$ = 25–30 °C, $RH_{a,o}$ increases due to

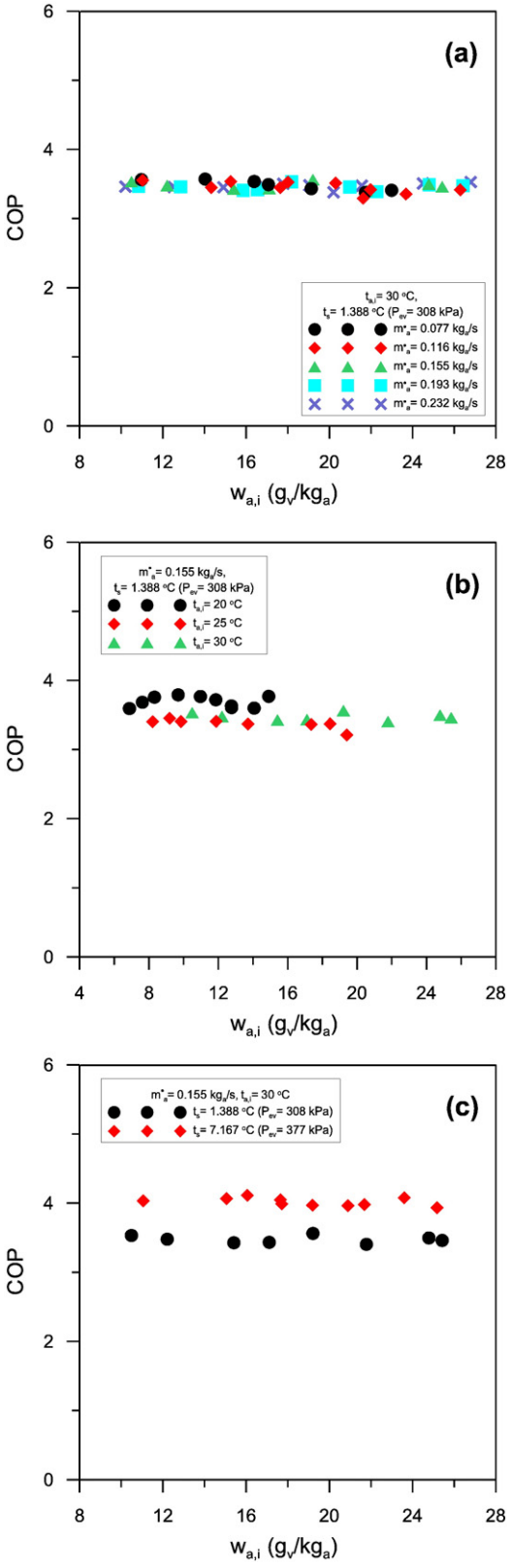

Fig. 11. Variation of coefficient of performance against air inlet specific humidity: (a) Effect of air mass flow rate (b) Effect of evaporator air inlet temperature and (c) Effect of evaporator saturation temperature.

re-evaporation of water condensate part as a result in the increase of $t_{a,i}$. The effect of t_s on $t_{a,o}$ and $RH_{a,o}$ is clear where $t_{a,o}$ decreases and $RH_{a,o}$ increases as t_s increases. This is due to the increase of evaporator superheated region with dropping of t_s at constant total evaporator refrigeration capacity and this leads to rising of $t_{a,o}$ and consequently dropping of $RH_{a,o}$ as can be seen in Fig. 12e and f.

For instances, the minimum and maximum amount of fresh water production rate and their corresponding supplied air conditions to conditioned space can be obtained from Fig. 12c–d at $m^{\cdot}_a = 0.155$ kg/s, $t_s = 7.167$ °C and $t_{a,i} = 20$–30 °C. As shown in the figure, at $t_{a,i} = 20$ °C, the minimum and maximum of fresh water production rate and supplied air conditions are $m^{\cdot}_w = 0.93$ and 3.14 kg/h, $t_{a,o} = 13.85$ and 17.38 °C, $RH_{a,o} = 63$ and 68%, respectively. Moreover, at $t_{a,i} = 25$ °C, the minimum and maximum of fresh water production rate and supplied air conditions are $m^{\cdot}_w = 1.77$ and 4.74 kg/h, $t_{a,o} = 17.35$ and 22.71 °C, $RH_{a,o} = 45$ and 57%, respectively. Furthermore, at $t_{a,i} = 30$ °C, the minimum and maximum of fresh water production rate and supplied air conditions are $m^{\cdot}_w = 2.35$ and 6.13 kg/h, $t_{a,o} = 22.47$ and 27.24 °C, $RH_{a,o} = 59$ and 69%, respectively. Fig. 13 shows the limits of supplied air conditions ($t_{a,o}$ and $RH_{a,o}$) at any fresh water production rate ($m^{\cdot}_w$) for all studied parameter ranges of the proposed system.

4.5. Evaluation of the suggested hybrid system

It is observed from the above analysis that, the recommended operating conditions for the proposed hybrid system can be evaluated in terms of space-supplied air conditions and the amount of fresh water production rate. Fig. 14 shows all available space-supplied air conditions obtained from proposed system located on the Psychrometric chart relative to human comfort condition. As shown in the figure, the applicable space-supplied air conditions region is bounded with $t_{a,o} = 9$–22 °C and $w_{a,o} = 4$–10 g_v/kg_a, where the conditions which located outside this region aren't desirable.

Clearly, the proposed system can operate under $t_{a,i} = 25$ °C, $w_{a,i} = 8.8$ g_v/kg_a, $m^{\cdot}_a = 0.155$ kg/s and $t_s = 7.167$ °C to supply $t_{a,o} = 17.35$ °C, $RH_{a,o} = 45\%$ and $m^{\cdot}_w = 1.77$ kg/h. These supply conditions are sufficient for conventional air conditioning systems according to the proposed accepted region as shown in Fig. 14. On the other hand, the system can operate under $t_{a,i} = 25$ °C, $w_{a,i} = 18.7$ g_v/kg_a, $m^{\cdot}_a = 0.155$ kg/s and $t_s = 7.167$ °C to supply $t_{a,o} = 22.71$ °C, $RH_{a,o} = 57\%$ and $m^{\cdot}_w = 4.74$ kg/h which is suitable for air conditioning using under floor air distribution system (UFAD). Additionally, in order to attain human thermal comfort, the proposed hybrid system can be operated in case of $t_{a,i} = 20$ °C, $m^{\cdot}_a = 0.155$ kg/s and $t_s = 7.167$ °C and $w_{a,i} = 6.9$ and 14 g_v/kg_a to supply $t_{a,o} = 13.85$ and 17.38 °C, $RH_{a,o} = 63$ and 68%, respectively by using heating and/or humidification processes downstream the evaporator.

5. Experimental correlations

Fig. 15a–f shows different predicted correlations and their errors for ($m^{\cdot}_w/m^{\cdot}_{a,max}$), ($Q^{\cdot}_{ref}/Q^{\cdot}_{ref,max}$) and (($W^{\cdot}_c/m^{\cdot}_w$)/$h_{fg,0\ °C}$) in terms of the various operating parameters that employed in the present study (i.e. Re_{Dh}, $w_{a,i}$, w_s, $t_{a,i}$ and t_s). The experimental data are regressed in the following ranges: $287 \le Re_{Dh} \le 1045$, $5.6\ g_v/kg_a \le w_{a,i} \le 27.7\ g_v/kg_a$, $4.19\ g_v/kg_a \le w_s \le 6.4\ g_v/kg_a$, $20\ °C \le t_{a,i} \le 30\ °C$, $1.388\ °C \le t_s \le 7.167\ °C$.

Fig. 14a shows the predicted dimensionless form of fresh water production rate in terms of operating parameters as follows:

$$\frac{m^{\cdot}_w}{m^{\cdot}_{a,\max}} = 6.735 \times 10^{-6}\ Re_{hD}^{0.88} \left(\frac{w_{a,i}}{w_s}\right)^{1.23} \left(\frac{t_{a,i}}{t_s}\right)^{-0.28}. \quad (10)$$

Eq. (10) can predict 85% of the experimental results within error of ±25% as illustrated in Fig. 15b. The correlation shows that the fresh water production rate is directly proportional to Reynolds number and air inlet specific humidity and reversely proportional to air inlet temperature. Another dimensionless correlation for total evaporator

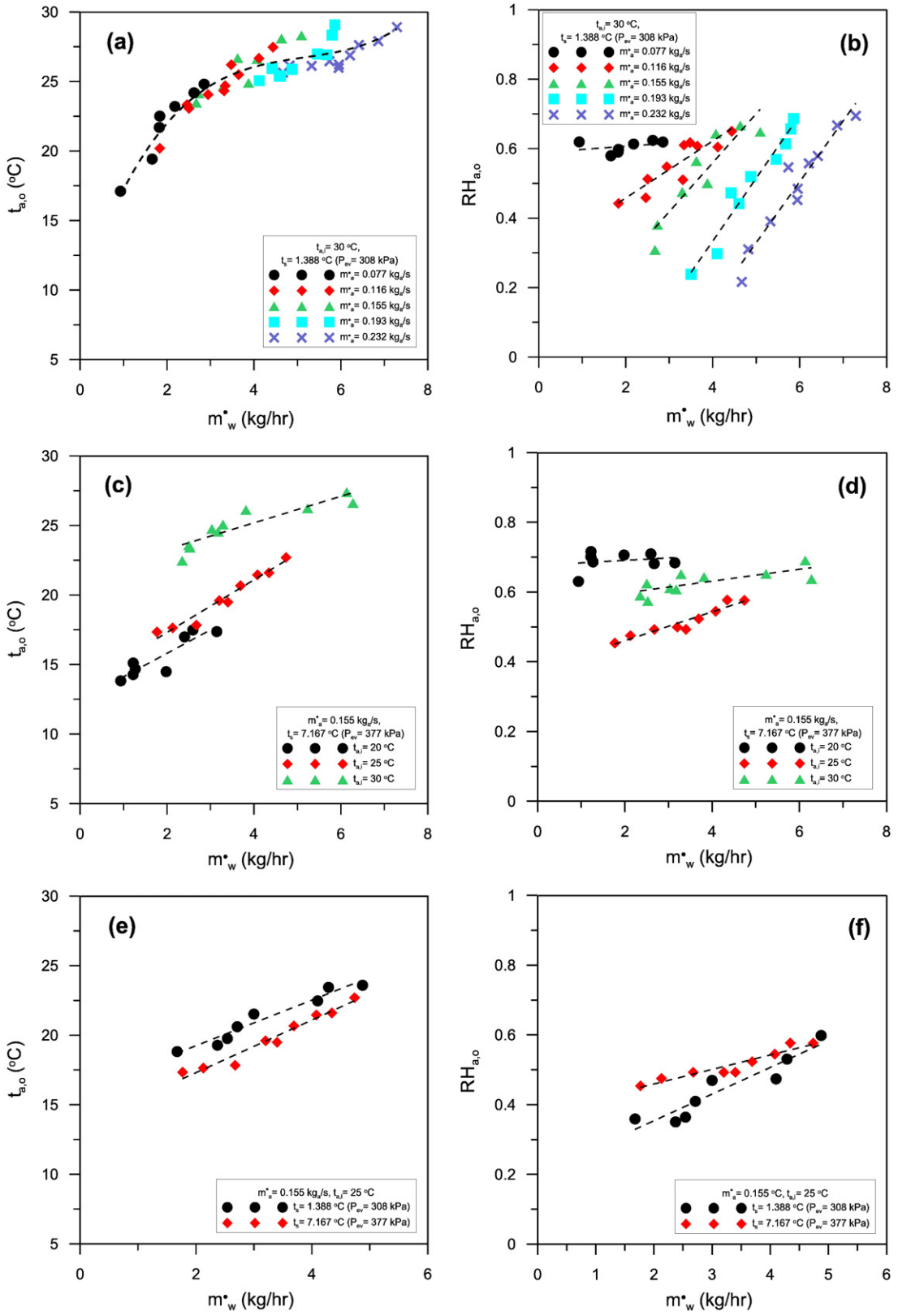

Fig. 12. Variation of conditioned space-supplied air conditions against fresh water rate for $w_{a,i} = 5.6–27.7\ g_v/kg_a$: (a) and (b) Effects of air mass flow rate, (c) and (d) Effects of evaporator air inlet temperature, and (e) and (f) Effects of evaporator saturation temperature.

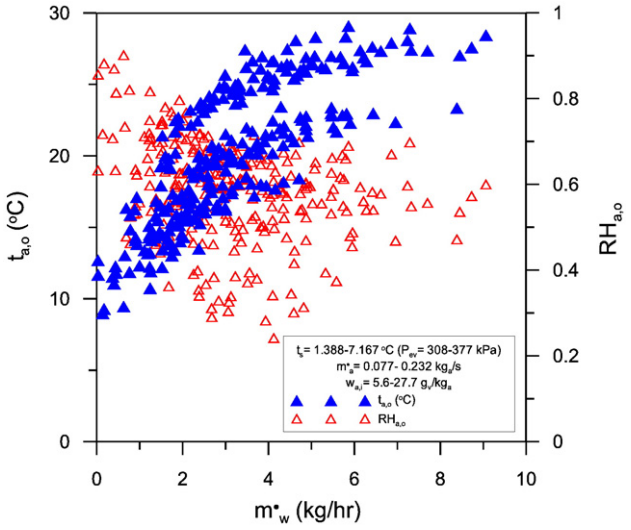

Fig. 13. Space-supplied air conditions against produced fresh water rate.

refrigeration capacity is shown in Fig. 15c. The predicted correlation is derived in the same way of Eq. (10) as follows:

$$\frac{\dot{Q}_{ref}}{\dot{Q}_{ref,\max}} = 2.76\times10^{-3}\mathrm{Re}_{hD}^{\ 0.72}\left(\frac{w_{a,i}}{w_s}\right)^{0.78}\left(\frac{t_{a,i}}{t_s}\right)^{-0.16}. \tag{11}$$

Eq. (11) can predict 84% of the experimental data within error ± 20% as presented in Fig. 15d. Additionally, the correlation shows that the total evaporator refrigeration capacity is directly proportional to Reynolds number and air inlet specific humidity and reversely proportional to air inlet temperature. Furthermore, dimensionless correlation for compressor work is presented in Fig. 15e and it is given as follows:

$$\frac{\left(\dot{W}_c/\dot{m}_w\right)}{h_{fg,0^\circ C}} = 1.63\mathrm{Re}_{hD}^{\ -0.2}\left(\frac{w_{a,i}}{w_s}\right)^{-0.57}\left(\frac{t_{a,i}}{t_s}\right)^{0.19}. \tag{12}$$

Eq. (12) can predict 95% of the experimental data within error ± 15% as presented in Fig. 15f. Moreover, the correlation illustrates that the compressor power is directly proportional to air inlet temperature and reversely proportional to Reynolds number and air inlet specific humidity.

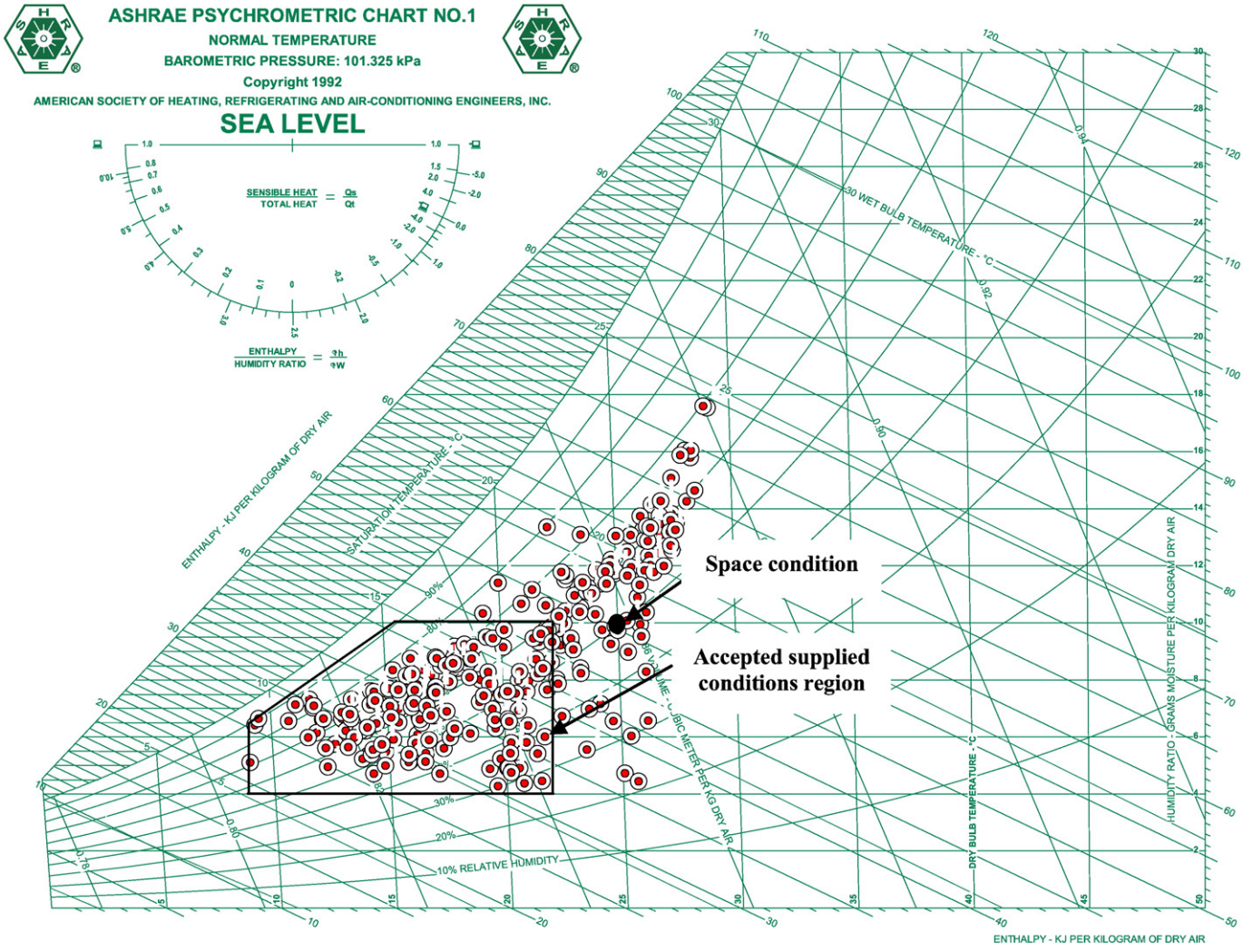

Fig. 14. Space-supplied air conditions on Psychrometric chart.

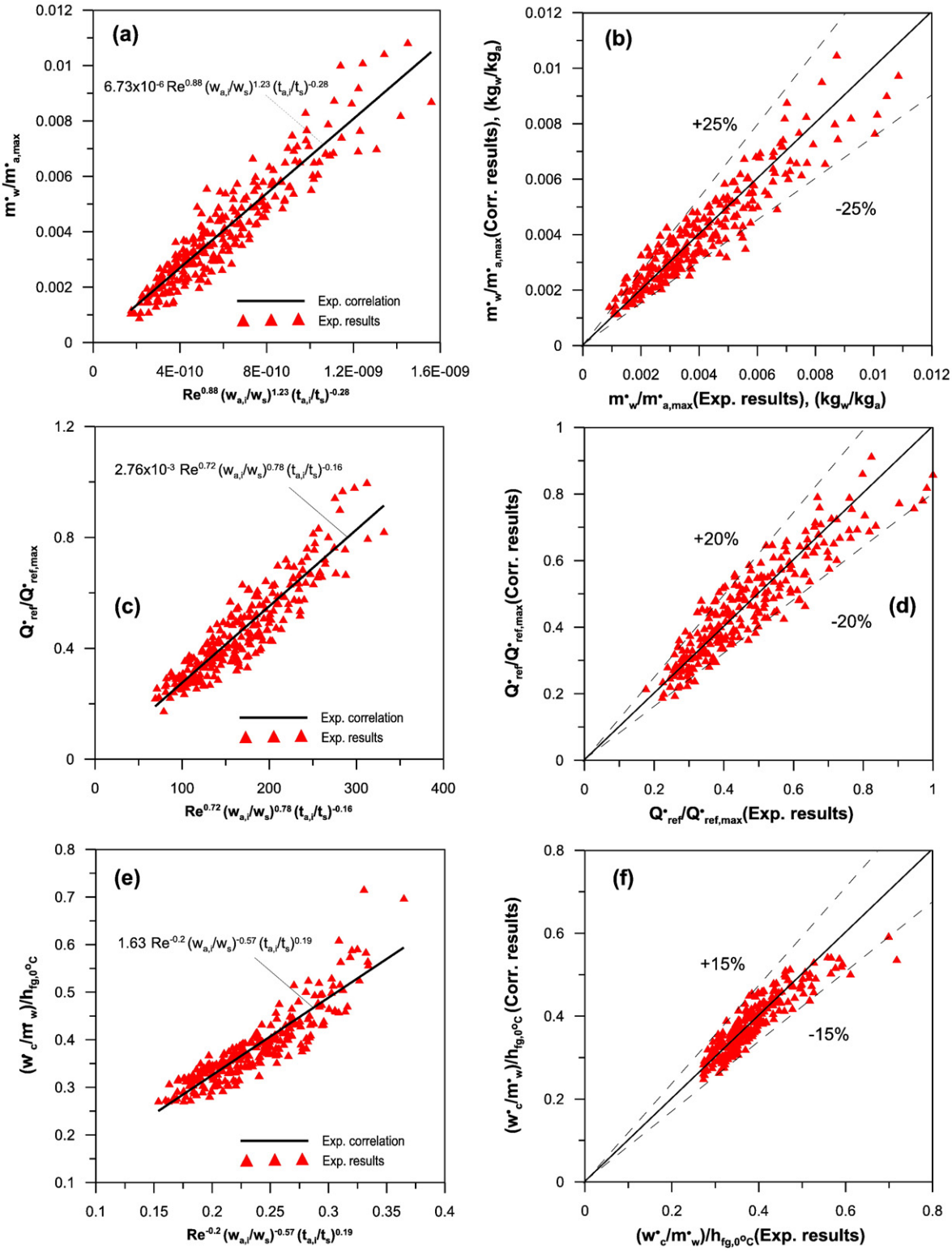

Fig. 15. Experimental correlations prediction and errors: (a) ($\dot{m}^{\bullet}_{w}/\dot{m}^{\bullet}_{a,max}$), (c) ($\dot{Q}^{\bullet}_{ref}/\dot{Q}^{\bullet}_{ref,max}$) (e) (($\dot{W}^{\bullet}_{c,act}/\dot{m}^{\bullet}_{w}$)/$h_{fg,0\ ^{\circ}C}$) and (b),(d), and (f) Errors.

6. Conclusions and recommendations

Experimental study for investigating humidification–dehumidification water desalination and air conditioning system using vapor compression refrigeration cycle has been carried out. The influences of system operating parameters (air mass flow rate, air inlet temperature, air inlet specific humidity and the evaporator saturation temperature) on desalinated water production rate, evaporator refrigeration capacity, compressor work per kilogram of fresh water, mass transfer coefficient and conditioned space-supplied air conditions (air temperature and relative humidity) were studied and presented. The conclusions obtained from the present study are listed briefly as follows:

- The desalinated water production rate and total evaporator refrigeration capacity enhance with increasing the air specific humidity, air inlet temperature in the (20 °C ≤ $t_{a,i}$ ≤ 25 °C), and significant increase

was obtained at $t_{a,i} = 25$ °C and 30 °C with increasing air mass flow rate.

- The mass transfer coefficient decreases with increasing air specific humidity, evaporator air inlet temperature in the (20 °C ≤ $t_{a,i}$ ≤ 25 °C), and significant decrease was obtained at $t_{a,i} = 25$ °C and 30 °C with increasing air mass flow rate.
- The desalinated water production rate and mass transfer coefficient decrease with increasing evaporator air inlet temperature ($t_{a,i} > 25$ °C).
- $Q^{\bullet}_{ref}$ augments with rising the air specific humidity and air mass flow rate, evaporator saturation temperature and evaporator air inlet temperature.
- Compressor work per kilogram of fresh water decreases with increasing the air specific humidity, air mass flow rate and evaporator saturation temperature and decreasing air inlet temperature.
- Air mass flow rate and evaporator air inlet temperature have a considerable influence on the $t_{a,o}$ and $RH_{a,o}$, where $t_{a,o}$ rises and $RH_{a,o}$ drops as $m^{\bullet}_{a}$ and $t_{a,i}$ (20–25 °C) increase.
- The system desired output quantities can be obtained at $t_{a,i} = 25$ °C, where, the minimum and maximum of fresh water production rate and supplied air conditions are $m^{\bullet}_{w} = 1.77$ and 4.74 kg/h, $t_{a,o} =$ 17.35 and 22.71 °C, $RH_{a,o} = 45$ and 57%, respectively.
- Dimensionless correlations for desalinated fresh water production rate, evaporator total refrigeration capacity and compressor power in terms of various operating parameters that employed in the present study were correlated and presented within acceptable error.

References

[1] R.V. Wahlgren, Atmospheric water vapor processor designs for potable water production; a review, Water Res. 35 (1) (2001) 1–22.
[2] Narmine H. Aly, Adel K. El-Fiqi, Mechanical vapor compression desalination systems—a case study, Desalination 58 (1) (2003) 43–150.
[3] J. Siqueiros, F.A. Holland, Water desalination using heat pumps, Energy 25 (2000) 717–729.
[4] M.N.A. Hawlader, P.K. Dey, S. Diab, Solar assisted heat pump desalination system, Desalination 168 (2004) 49–54.
[5] V.V. Slesarenko, Heat pumps as a source of heat energy for desalination of seawater, Desalination 139 (2001) 405–410.
[6] F. Al-Juwayhel, H. El-Dessouky, H. Ettouney, Analysis of single effect evaporator desalination systems combined with vapor compression heat pumps, Desalination 114 (1997) 253–275.
[7] P. Gao, L. Zhang, H. Zhang, Performance analysis of a new type desalination unit of heat pump with humidification and dehumidification, Desalination 220 (2008) 531–537.
[8] G. Yuan, L. Zhang, H. Zhang, Experimental research of an integrative unit for air conditioning and desalination, Desalination 182 (2005) 511–516.
[9] B.A. Habeebullah, Performance analysis of a combined heat pump-dehumidifying system, JKAU Eng. Sci. 21 (1) (2010) 97–114.
[10] M.V. Rane, Y.S. Padiya, Heat pump operated freeze concentration system with tubular heat exchanger for seawater desalination, Energy Sustain. Dev. 15 (2011) 184–191.
[11] Jinzeng Chen, Suyi Huang, A discussion of "Heat pumps as a source of heat energy for desalination of seawater", Desalination 169 (2004) 161–165.
[12] M. Zamen, S.M. Soufari, S. Abbasian Vahdat, M. Amidpour, M.A. Zeinali, H. Izanloo, H. Aghababaie, Experimental investigation of a two-stage solar humidification–dehumidification desalination process, Desalination 332 (2014) 1–6.
[13] Mohammed A. Al-Weshahi, Alexander Anderson, Guohong Tian, Organic Rankine cycle recovering stage heat from MSF desalination distillate water, Appl. Energy 130 (2014) 738–747.
[14] Hanen Ben Halima, Nader Frikha, Romdhane Ben Slama, Numerical investigation of a simple solar still coupled to a compression heat pump, Desalination 337 (2014) 60–66.
[15] Xinhua Li, Experimental Analysis of Produced Water Desalination by a Humidification–Dehumidification Process, Department of Petroleum Engineering, Socorro, New Mexico, 2009. (Master theses, November).
[16] Shaobo Houa, Huacong Lia, Hefei Zhanga, An open air–vapor compression refrigeration system for air-conditioning and desalination on ship, Desalination 222 (2008) 646–655.
[17] A.S. Huzayyin, S.A. Nada, H.F. Elattar, Air-side performance of a wavy-finned-tube direct expansion cooling and dehumidifying air coil, Int. J. Refrig. 30 (2007) 230–244.
[18] Jiubing Shen, Ziwen Xing, Xiaolin Wang, Zhilong He, Analysis of a single-effect mechanical vapor compression desalination system using water injected twin screw compressors, Desalination 333 (2014) 146–153.
[19] M.T. Ghazal, U. Atikol, F. Egelioglu, An experimental study of a solar humidifier for HDD systems, Energy Convers. Manag. 82 (2014) 250–258.
[20] A.A. Attia, New proposed system for freeze water desalination using auto reversed R-22 vapor compression heat pump, Desalination 254 (2010) 179–184.
[21] Ahmad Al-Ansari, Hisham Ettouney, Hisham El-Dessouky, Water–zeolite adsorption heat pump combined with single effect evaporation desalination process, Renew. Energy 24 (2001) 91–111.
[22] A.S. Nafey, H.E.S. Fath, S.O. El-Helaby, A.M. Soliman, Solar desalination using humidification dehumidification processes. Part I. A numerical investigation, Energy Convers. Manag. 45 (2004) 1243–1261.
[23] A.S. Nafey, H.E.S. Fath, S.O. El-Helaby, A.M. Soliman, Solar desalination using humidification dehumidification processes. Part II. An experimental investigation, Energy Convers. Manag. 45 (2004) 1263–1277.
[24] J. Roy Dossat, Principles of Refrigeration, 4th ed. John Wiley & Sons, 1996.
[25] A. Piacentino, M. Talamo, Innovative thermoeconomic diagnosis of multiple faults in air conditioning units: methodological improvements and increased reliability of results, Int. J. Refrig. 36 (8) (2013) 2343–2365.
[26] ASHRAE, ASHRAE Handbook HVAC Systems and Equipment, American Society of Heating, Refrigeration and Air-conditioning Engineers, Inc., Atlanta, GA, 2004.
[27] J.P. Holman, W.J. Gajda, Experimental Method for Engineers, McGraw Hill, New York, 1994..